

True random number generation using 1T' molybdenum ditelluride

Authors

Yang Liu^{1,2}, Pengyu Liu¹, Yingyi Wen¹, Zihan Liang³, Songwei Liu¹, Lekai Song¹, Jingfang Pei¹, Xiaoyue Fan⁴, Teng Ma⁵, Gang Wang⁴, Shuo Gao⁶, Kong-Pang Pun¹, Xiaolong Chen³, Guohua Hu^{1,*}

Affiliations

¹Department of Electronic Engineering, The Chinese University of Hong Kong, Shatin, N. T., Hong Kong S. A. R., China

²Shun Hing Institute of Advanced Engineering, The Chinese University of Hong Kong, Shatin, N. T., Hong Kong S. A. R., China

³Department of Electrical and Electronic Engineering, Southern University of Science and Technology, Shenzhen, 518055, China

⁴School of Physics, Beijing Institute of Technology, Haidian, Beijing, 10081 China

⁵Department of Applied Physics, Hong Kong Polytechnic University, Hung Hom, Kowloon, Hong Kong S. A. R., 999077, China

⁶School of Instrumentation and Optoelectronic Engineering, Beihang University, Beijing 100191, China

*Correspondence to: ghhu@ee.cuhk.edu.hk

Abstract

True random numbers are essential for scientific research and various engineering problems. Their generation, however, depends on a reliable entropy source. Here, we present true random number generation using the conductance noise probed from structurally metastable 1T' MoTe₂ prepared via electrochemical exfoliation. The noise, fitting a Poisson process, is a robust entropy source capable of remaining stable even at 15 K. Noise spectral density and statistical time-lag suggest the noise originates from the random polarization of the ferroelectric dipoles in 1T' MoTe₂. Using a simple circuit, the noise allows true random number generation, enabling their use as the seed for high-throughput secure random number generation over 1 Mbit/s, appealing for applications such as cryptography where secure data protection has now become severe. Particularly, we demonstrate safeguarding key biometric information in neural networks using the random numbers, proving a critical data privacy measure in big data and artificial intelligence.

Main text

Random numbers, a string of random bits, play a crucial role in scientific research and engineering problems, for example, serving as the random input in numerical simulations and modelling, and introducing uncertainty in gaming and decision-making ^[1]. Random numbers can typically be generated by deterministic algorithms ^[2], and these random numbers are thus essentially pseudo-random numbers ^[2]. As the demand for true randomness by applications is increasingly stringent, the need for true random numbers has become critical ^[3]. True random numbers, derived from physical entropy sources such as thermal noise and random telegram noise ^[4], exhibit inherent randomness and cannot be predicted or reproduced ^[4]. However, harnessing these entropy sources can be energy-consuming, and they can be vulnerable to the ambient noise and cryogenic attacks, undermining their reliability for true random number generation ^[5].

Intriguingly, advances in nanomaterials present new promising solutions for true random number generation. Quantum phenomena widely observed in nanomaterials, such as quantum tunnelling and electron-phonon interactions, are proved inherently random ^[6-8] and may thus be harnessed for true random number generation. Among the various nanomaterials, 2D materials hold great interest for true random number generation for modern electronics, given their unique material properties and the possibility for integration and synergy with the modern electronics systems ^[9,10]. Particularly, with atomically thin structures and quantum confinements, 2D materials can exhibit random variations in their underlying electronic, optoelectronic, and photonic processes, as well as their atomic structures ^[11,12]. For example, molybdenum ditelluride (MoTe_2), a transition metal dichalcogenide, can exist in a prismatic-orthorhombic (2H-1T) intermediate octahedral 1T' phase in its mono- and few-layer forms ^[13]. The structural metastability can induce random polarization of the ferroelectric dipoles and, consequently, variations in the electronic structures and properties ^[14]. Prior studies show that the structural metastability can even be resilient to the ambient noise ^[15,16], manifesting the potential of using 1T' MoTe_2 for true random number generation.

In this work, we report true random number generation from electrochemical exfoliated 1T' MoTe_2 . We show the 1T' MoTe_2 allows stable conductance noise probing at low temperatures down to 15 K and, notably, fitting a Poisson process, the noise is proved random and a reliable entropy source. Our analysis of the noise spectral density and statistical time-lag suggest the noise can be attributed to the random polarization of the ferroelectric dipoles in 1T' MoTe_2 . With the characteristics, the noise allows true random number generation via a simple circuit design. This enables their use as the seed for high-throughput secure random number generation exceeding 1 Mbit/s, appealing for the practical applications. Here we apply the random numbers in cryptography. Particularly, we show safeguarding of key biometric information in neural networks by using the random numbers as the mask, proving a critical data privacy measure for big data and artificial intelligence where secure protection of data and privacy is now severe.

Conductance noise probing

MoTe_2 predominantly exhibits a stable semiconducting 2H phase ^[17], with the hexagonally bonded Mo atoms sandwiched between two planes of Te atoms (Fig. 1a). The 2H phase, however, can have local lattice distortion along the y -axis, with the Te atoms forming an octahedral coordination around the Mo atoms to give an alternating Te-Mo-Te stacking ^[18,19]. This leads to phase transition to a 2H-1T intermediate octahedral ferroelectric 1T' phase ^[18,19]. Different from 2H phase, the 1T' phase is structurally metastable and, consequently, random variations can render in the electronic structures and properties.

1T' MoTe₂ can be produced via physical and chemical engineering processes^[20,21]. Here we adopt the electrochemical exfoliation method reported in prior studies for 1T' MoTe₂ production (see Methods; Fig. 1b)^[22]. Briefly, molecular compounds intercalate between the MoTe₂ layers, leading to exfoliation and, importantly, distortion of the 2H crystalline structure. Figure 1c presents our solution of the exfoliated MoTe₂. We show in Fig. 1d, e the transmission electron microscopic (TEM) images of the exfoliated nanosheets. This proves MoTe₂ is successfully exfoliated and the nanosheets have minimal defects. Particularly, a lattice spacing of 3.4Å and a non-hexagonal structure are revealed, indicating that the exfoliated MoTe₂ is in the 1T' phase^[23]. Further electron diffraction pattern (Fig. 1e inset) shows a non-hexagonal rhombic, tetragonally symmetric lattice, confirming the 1T' phase. Meanwhile, to verify the minimal defects in the exfoliated 1T' MoTe₂, we perform X-ray photoelectron spectroscopic (XPS) analysis and prove a ~1:2 ratio for the Mo and Te atoms (Fig. S1). The minimal defects can be ascribed to the use of molecular compounds for intercalation as the large molecular size can effectively expand the bulk MoTe₂ for exfoliation while limiting the intercalations^[22]. Notably, the minimal defects suggest that the 1T' phase primarily arises from intercalation-induced lattice distortion rather than the defects.

The structural metastability in the 1T' phase MoTe₂ may lead to random variations in the electrical properties. To probe the variations, we fabricate very simple vertically structured devices, where the 1T' MoTe₂ is sandwiched between the top and bottom electrodes (Fig. S2). See the fabrication in Methods. This simple device structure can allow convenient electrical characterization. We show in Fig. 2a the current-voltage output from a typical device under sweeping bias, proving random variations in the device resistance switching (switching ratio ~10³). The random variations prove the randomly varying electrical conductivity of the 1T' MoTe₂ and, particularly, the switching (at ~5 V) suggests a further crystalline structure distortion towards a metallic 1T phase^[21] or a potential conductivity modulation by the electrostatic Stark effect reported in prior studies^[24,25]. Nevertheless, the random variations may be harnessed as an entropy source for true random number generation. However, for convenient device operation and random variation harnessing, we measure the current output from the 1T' MoTe₂ devices under static bias instead of sweeping bias, and probe the random variations exhibited in the current output.

We first study the current output at room temperature. Figure 2b shows the current output from a typical device at 0.05 V, 300 K (see also the current output at 0.1-5 V in Fig. S3a-h). As observed, featureless, random yet stable variations are demonstrated in the current output at all the bias conditions. For simplicity, we refer to the variations in the current output as the conductance noise. The conductance noise can be considered as an indication of the random variations in the electrical conductivity of the 1T' MoTe₂. To assess the conductance noise, we plot the histograms of the current data points in Fig. 2d (see also Fig. S3i-p) and fit the histograms to Poisson distributions. As shown, the histograms all can well fit a Poisson process, proving that the current data points all occur independently of the others. This means that the conductance noise is a random process and a reliable entropy source^[26]. Note that a Poisson process describes a system consisting of objects randomly distributed with the essential feature that the objects occur independently of one another^[27]. Given the potential exposure to cryogenic attacks in the practical applications of true random numbers, we extend the assessment to low and even cryogenic temperatures (Fig. 2c). As shown, featureless, random yet stable conductance noise is proved at all the low temperatures. Meanwhile, notably, the conductance noise all can fit a Poisson process (Fig. 2e-g). Therefore, the investigation proves that the conductance noise is a reliable entropy source capable of remaining stable even at cryogenic temperatures.

The noise from thermal and electronic systems typically stands as a primary entropy source for true random number generation^[28]. To exclude the possibility that the conductance noise is the ambient noise from thermal and the electrical characterization system, we concurrently test a blank device. As clearly shown by the grey current output in Fig. 2b, c, the ambient noise distinctly deviates from the conductance noise (smaller by several orders of magnitude). Therefore, even taking the interference from the ambient noise into account, the origin of the conductance noise is primarily attributed to the material property of the 1T' MoTe₂.

Origin of the conductance noise

To study the origin of the conductance noise, we perform current power spectral density (PSD) characterization of the 1T' MoTe₂ device at varying testing conditions of bias and temperature (Fig. 3a-d, Fig. S4). As demonstrated, the PSD testing in general proves 1/f noise over a broad frequency. For example, at 0.05 V, 300 K, the noise spectral power well fits 1, i.e. $\gamma \sim 1$, proving a 1/f noise (Fig. 3c). However, as the frequency increases, the output is flattened, indicating thermal noise and/or other high-frequency noise dominate the high frequency region (Fig. 3d). Flattening at the high frequency regions for the low bias conditions may be due to the insufficient current signals^[29,30]. Nevertheless, 1/f noise is proved for the 1T' MoTe₂ device. This suggests charge fluctuations may account for the conductance noise, for instance, charge trapping and de-trapping at the defect sites^[31,32]. Charge trapping and de-trapping is a major mechanism for 1/f noise and has been widely exploited as the entropy source for true random number generation^[31,33]. However, as demonstrated, varying the bias and temperature do not lead substantially changes of the 1/f noise, suggesting that charge trapping and de-trapping by defects may not account for the 1/f noise. Indeed, as discussed, our 1T' MoTe₂ is proved to have minimal defects. This leads us to conclude that the conductance noise arises from the intrinsic material property of 1T' MoTe₂. Given the structurally metastability of ferroelectric 1T' MoTe₂, we assume the conductance noise arises from the random polarization of 1T' MoTe₂. However, polarization testing of the 1T' MoTe₂ device (Fig. S5) shows no clear evidence of ferroelectric polarization. The polarization may have been compromised by the discrete nature of the electrochemical exfoliated 1T' MoTe₂ nanosheets^[34]. With this consideration, we hypothesize the conductance noise arises from the random polarization of the underlying ferroelectric dipoles in 1T' MoTe₂.

To investigate our hypothesis further, we study the cumulative charge characteristic of the MoTe₂ device. Here we plot in Fig. 3e the current output of the MoTe₂ device at 0.05 V, 300 K and the corresponding cumulative charge integrated in the sampling time interval. Note the cumulative charge state may correspond to the polarization state of the ferroelectric dipoles in the 1T' MoTe₂^[35]. As observed, the cumulative charge proves a featureless, random yet stable noise, indicating the noise in the polarization states. Here we adopt a weighted time-lag method to statistically evaluate this noise. Note weighted time-lag is a method widely used to study the random telegraph noise characteristics^[36]. Briefly, as plotted in Fig. 3f, the distribution of the cumulative charge is defined with a weighted time-lag, $TL = \lg \left(K \sum_n^{N-1} \frac{1}{2\pi\alpha^2} \exp \left(-\frac{[(Q_n-x)^2+(Q_{n+1}-y)^2]}{2\alpha^2} \right) \right)$, where Q_n and Q_{n+1} are the cumulative charge states at the n -th and $(n+1)$ -th moments, (x, y) denotes the corresponding coordinates in the TL plot, N is the total number of the moments, and α and K are the fitting parameters to ensure that the maximum of the TL plot before logarithm equals to 1. The cumulative charge states in the plot are distributed in an ascending order, and a TL approaching 0 means a stronger correlation between the cumulative charge state with the next state. As observed, the TL plot shows random yet uniform aggregations with a bimodal distribution

along the diagonal – both the larger and smaller cumulative charge states establish stronger correlations with their next states, while the medium cumulative charge states show weaker correlations. This indicates that the ferroelectric dipoles are uniformly distributed with bimodal aggregations, and that the strongly polarized dipoles may require a stronger current and a longer time to reverse. Meanwhile, the noise suggests the random polarization of the ferroelectric dipoles in the 1T' MoTe₂.

See also the cumulative charge profiles and *TL* plot patterns from a blank device and a device fabricated with liquid-phase exfoliated MoS₂ in Fig. S6. Similar to MoTe₂, MoS₂ is transition metal dichalcogenide, but it is structurally stable with a 2H phase^[37]. The blank device shows noise from the ambient, such as the thermal noise and the possible noise from the electrical characterization system. The *TL* plot establishes monostable aggregation with weak correlations in the cumulative charge states, meaning weak correlation in the noise states from the blank device. The MoS₂ device shows distinct random telegraph noise (RTN) with random switching, as reported in prior studies^[31,33]. RTN is suggested to arise from charge trapping and de-trapping at the defect sites in MoS₂^[31,33]. Very distinctively, the *TL* plot establishes aggregation regions with strong correlations in the corresponding cumulative charge states, which may be a result of the charge trapping and de-trapping. Therefore, the comparison of the 1T' MoTe₂ device to the blank device and the MoS₂ device further supports our hypothesis that the conductance noise originates from the random polarization of the underlying ferroelectric dipoles in 1T' MoTe₂.

We schematically illustrate the random polarization of the ferroelectric dipoles in 1T' MoTe₂ in Fig. 3g. Here we conduct Monte Carlo simulation of the random polarization of the ferroelectric dipoles (see Methods). Based on our hypothesis, we assume that the ferroelectric dipoles in 1T' MoTe₂ are uniformly distributed, and that the ferroelectric dipoles undergo random polarizations. Upon electrical characterization of the 1T' MoTe₂ device with a static bias, the random polarization of the ferroelectric dipoles can lead to fluctuations in the bound charges and thus the conductance noise. As studied by the Monte Carlo simulation, the current output is stable over a prolonged period with featureless, random yet stable noise, consistent with the experiment results (Fig. 3h). Meanwhile, the conductance noise also fits a Poisson process (Fig. 3i). Therefore, the Monte Carlo simulation from the perspective of dipole moment fluctuations concludes that the conductance noise may arise from the random polarization of the ferroelectric dipoles in 1T' MoTe₂ and that the conductance noise is a reliable entropy source.

True random number generation

To harness the conductance noise for true random number generation, we design a simple circuit via Cadence Virtuoso as illustrated in Fig. 4a, b. Briefly, the circuit consists of a 1T' MoTe₂ device, an I/V converter, a high pass filter, a voltage amplifier, and a comparator. Upon operation, the I/V converter transforms the current output from the 1T' MoTe₂ device into a voltage output. Voltage signals are more convenient for the subsequent signal processing. As shown in Fig. 4c, the voltage signal, i.e. '*Output 1*', demonstrates a voltage profile with featureless, random yet stable noise. The voltage noise fits a Poisson process (Fig. 4d). This proves that the circuit has captured the conductance noise from the 1T' MoTe₂ and that the voltage signal with the noise is well suited to true random number generation. The voltage signal is then passed through the high-pass filter and the voltage amplifier to extract the noise in the form of differentiated voltage spikes, as shown by '*Output 2*' and '*Output 3*' in Fig. 4c. As demonstrated, the voltage spikes also fit a Poisson process (Fig. 4e, f), proving that the extracted noise remains as a reliable entropy source for true random

number generation. The comparator then processes the voltage spikes to yield random numbers in the form of 0's and 1's binary digit strings, as shown by the 'Output 4' in Fig. 4c (see Fig. S7 for a zoomed-in distribution of the 0's and 1's digits). As demonstrated, the random numbers are consisted of random 0's and 1's digits, with a ratio of $\sim 1:1$ (Fig. 4g). This suggests that the random numbers generated from the circuit are random and potentially useful for practical applications.

To verify the random numbers generated are truly random, we test their randomness using the National Institute of Standards and Technology (NIST) randomness testing suite. The NIST randomness testing is widely used in the field to evaluate the randomness and unpredictability of random number generators [38]. As demonstrated in Table S1, the random numbers generated successfully pass the randomness test without post-processing, proving their true randomness and that the random numbers can be assessed as true random numbers. However, the throughput of the true random numbers is only approximately 10 bit/s, limiting the use in the practical applications that require high-throughput secure random numbers.

To address this limitation, employing a common approach for high-throughput random number generation in the field [39], we use the true random numbers as the seed, and then introduce the seed to a Non-Linear Feedback Shift Register (NLFSR) for high-speed output of random numbers with a data rate of, say, 1 Mbit/s, as shown in Fig. 4a, b. See the circuit design of the NLFSR in Fig. S8. Here, as a case example, we present a random number bitmap generated with the 1 Mbit/s high-throughput random numbers in Fig. S9. Also, importantly, as demonstrated in Table S2, the high-throughput random numbers fully pass the NIST randomness test.

Safeguarding neural networks

High-throughput secure random numbers with the sufficient randomness and a generation speed exceeding 1 Mbit/s fit the general practical applications [3]. As an example, here we apply the high-throughput random numbers in cryptographic applications. Cryptography is of critical importance in the current age with the data exponentially growing and at the risk of being attacked and sabotaged [3]. We show in Fig. S10 the generation of one-time and strongly randomized passwords using the random numbers. Besides, we demonstrate in Fig. S11 the use of the random numbers in encryption of video and audio. Briefly, the encryption begins with integrating the random numbers into an encryption algorithm (e.g. AES) to produce a unique key for encryption [40], and the encryption key is then used to encrypt (and decrypt) the data. The effectiveness of data encryption lies on the unpredictability of the encryption key, i.e. the random numbers [41].

Beyond the common cryptographic applications, the importance of cryptography using the random numbers is magnified by the rapid advancements of neural networks. Neural networks are widely used to undertake tasks in, for instance, image recognition, sensing and robotics, autonomous driving, manufacturing, and monitoring, where sensitive data can be constantly involved. Particularly, in the context of big data and artificial intelligence, sensitive biometric information such as retinas, facial characteristics, fingerprints, and even DNA can be excessively used and also potentially leaked and attacked. Secure protection of data and privacy has therefore become a critical issue, and adversarial data leakage and attacks in neural networks pose a significant threat to personal data privacy [42]. Here we adopt a differential data safeguarding strategy and investigate its effectiveness to obfuscate sensitive data in neural networks [42]. As schematically shown in Fig. S12, the differential safeguarding framework injects random numbers as the noise to the target dataset for perturbation. Following this approach, we first train a Residual neural network (Resnet)

model for pet cat recognition (Fig. 5a; see Methods). Resnets are a widely used neural network framework in image and pattern recognition^[43]. After training, the model performs successful pet recognition with an accuracy of 92%. See the confusion matrix and detailed performance including the training and validation accuracy and loss of the well-trained Resnet variant model in Fig. S13.

We then inject the random numbers as noise to the target validation data. Interestingly, as shown in Fig. 5a, taking the image of a Siamese cat for demonstration, the noise perturbation appears negligible to the human eyes, manifesting the random numbers as minor and almost imperceptible noise perturbation to the data. This is ascribed to the innate ability of the human brain to process visual information holistically, i.e. focusing on the broader picture rather than the minute details^[44]. However, as demonstrated in Fig. 5b, the noise perturbation substantially affects the recognition of the well-trained Resnet variant model at all the different convolution layers. The confusion matrix and the accuracy (~78%) demonstrate that the Resnet variant with the noise perturbation gives a relatively poor performance in recognition (Fig. 5c, d). See also Fig. S14 for the confusion matrix details with noise perturbation. Particularly, comparing the accuracies with and without the noise perturbation (Fig. 5d), a little noise perturbation can cause a substantial degradation in the classification accuracy. This is because the noise disrupts the feature detection capability of the well-trained Resnet variant model in the initial layers of the network, which is then propagated to the deeper layers, leading to the exacerbation of the error^[45]. The further detailed difference (i.e. Δ) between the two success rates in the different 37 categories can be found in Fig. 5e. The findings prove that injecting the random numbers as noise perturbations that are not discernible to the human eyes can substantially interfere with the neural networks and as such, enhance the security of the data privacy in neural networks.

Conclusion

In this work, we have reported true random number generation using structurally metastable 1T' MoTe₂. Our detailed characterizations and analysis suggest that the random polarization of the ferroelectric dipoles in 1T' MoTe₂ may give rise to conductance noise, and that the conductance noise can be easily harnessed as a reliable entropy source for true random number generation. Notably, the conductance noise can remain stable even at low temperatures down to 15 K, critical for the cryptogenic applications of true random numbers. We have proved true random number generation and their use as the seed for high-throughput random number generation exceeding 1 Mbit/s. High-throughput secure random numbers are appealing for various practical applications, for instance, cryptography. We have demonstrated data privacy safeguarding in neural networks using the random numbers. Neural networks pose a significant threat to personal data privacy, particularly the biometric information, in big data and artificial intelligence by adversarial data leakage and attacks. Our safeguarding approach can therefore serve as a critical data privacy measure. Given this, and the scalability as well as seamless integration with the electronics systems of the electrochemical exfoliated 1T' MoTe₂, our approach of true random number generation holds great potential towards enabling secure data privacy in neural networks.

Methods

Material production and device fabrication: Raw MoTe₂ and the other chemicals are purchased from Alpha Aesar and Sigma-Aldrich, and are used as received. The electrochemical exfoliation of MoTe₂ follows the method reported in Ref. (23). For device fabrication, the Au/MoTe₂/Au devices are fabricated on Si/SiO₂ wafer, where the MoTe₂ is deposited by spin coating, and the

gold electrodes are deposited by electron-beam evaporation. The electron-beam evaporator is IVS EB-600. The MoTe₂ after deposition is baked at 400 °C for 0.5 hours under nitrogen.

Electrical characterizations: Tektronix Keithley 4200-SCS parameter analyzer is used to measure the electrical characteristics of the devices under 300 K. For the 15 K, 100 K, and 200 K tests, FS-Pro is used under vacuum (~10⁻⁶ mbar).

Monte Carlo simulation: Assuming a constant electric field, the change in the polarization of the ferroelectric dipoles will not affect the field, but the internal polarization state of the ferroelectric dipoles in the 1T' MoTe₂ will change. The fluctuation of the polarization can lead to fluctuating bound charges, which can in turn cause fluctuations in the conductance state of the 1T' MoTe₂.

The polarization can switch between two states, i.e. P₁ and P₂, and the switching follows the Arrhenius law^[46]. The polarization can thus be modelled as a Poisson process, meaning that the probability of a switch in a small interval of time dt is given by $\lambda * dt$, where λ is the rate of the process. The rate follows the Arrhenius law, given by $\lambda = A * \exp(-E/(k * T))$, where A is the pre-exponential factor, E is the energy barrier, k is the Boltzmann constant, and T is the temperature. However, the switch in polarization now results in fluctuations in the bound charge instead of a change in the electric field. The bound charge ρ_B is related to the polarization P by the relation $\rho_B = -divP$, where div is the divergence operator, indicating that the bound charge is related to the spatial variation of the polarization. In a simple one-dimensional case, this can be described as $\rho_B = -dP/dx$. Now assume that the change in polarization is uniform across the material, the bound charge will change by $\Delta\rho_B$ proportional to the change in polarization ΔP , expressed as $\Delta\rho_B = -\Delta P/L$, where L is a characteristic length scale of the system. This change in voltage can cause a current to flow.

We propose that the change in the bound charge affects the resistance R of the material. A simple model assumes that the resistance is inversely proportional to the absolute value of the bound charge, $R = R_0/\rho_B$, where R_0 is a constant initial resistance. Finally, apply a constant voltage V across this variable resistor, the current I through the material at any time would be given by Ohm's law, $I(t) = V/R(t)$. The charge from the current can be described by $Q_i = \int_{t=i}^{t=i+1} dI/dt$. So every time the polarization switches, it will change the bound charge, which will then change the resistance and hence, the current fluctuations.

Consider a common effect often found in materials known as Poole-Frenkel behavior^[47], the current through the material (and hence the resistance) is affected by the applied electric field (which in our case can be linked to the bound charge), and the current density J is given by $J = J_0 * \exp(\beta * \sqrt{\varepsilon})$, where J_0 is the current density at zero field, ε is the electric field, and β is a material constant. In our scenario, we now link the bound charge and the electric field ε . Assume that the change in the bound charge $\Delta\rho_B$ is proportional to the change in electric field $\Delta\varepsilon$, the bound charge is expressed by $\Delta\rho_B = -\Delta\varepsilon/L$. Then, the current density will be dependent on the bound charge. Note that the $\sqrt{\varepsilon}$ means that this is not a simple linear or inversely proportional relationship.

Neural network recognition: The neural network security is carried out in Python 3 and is based on the Resnet framework. The Resnet variant is based on a Resnet 34 structure, consisting of

convolution layers, residual blocks, and so on. The information about the Resnet 34 can be found at: <https://pytorch.org/vision/main/models/generated/torchvision.models.resnet34.html>. The public dataset is from the Visual Geometry Group at the University of Oxford (available at <https://www.robots.ox.ac.uk/~vgg/data/pets/>). The dataset consists of a 37-category pet dataset with roughly 200 images for each class with different scales, poses, and lighting. All the images have an associated ground truth annotation of breed, head ROI, and pixel-level trimap segmentation, and those are used for training and testing.

References

1. Stipčević, M. & Koç, Ç. K. True Random Number Generators. in *Open Problems in Mathematics and Computational Science* (ed. Koç, Ç. K.) 275–315 (Springer International Publishing, Cham, 2014). doi:10.1007/978-3-319-10683-0_12.
2. Sparapani, R. Random Number Generation and Monte Carlo Methods (Second Edition). *J. Stat. Softw.* **11**, 1–2 (2004).
3. Yu, F. *et al.* A Survey on True Random Number Generators Based on Chaos. *Discrete Dyn. Nat. Soc.* **2019**, 1–10 (2019).
4. Pironio, S. *et al.* Random numbers certified by Bell’s theorem. *Nature* **464**, 1021–1024 (2010).
5. Soucarros, M., Clédière, J., Dumas, C. & Elbaz-Vincent, P. Fault analysis and evaluation of a true random number generator embedded in a processor. in *Journal of Electronic Testing* vol. 29 367–381 (2013).
6. Abraham, N., Watanabe, K., Taniguchi, T. & Majumdar, K. A High-Quality Entropy Source Using van der Waals Heterojunction for True Random Number Generation. *ACS Nano* **16**, 5898–5908 (2022).
7. Kim, G. *et al.* Self-clocking fast and variation tolerant true random number generator based on a stochastic mott memristor. *Nat. Commun.* **12**, 2906 (2021).
8. Liu, B. *et al.* Bi₂O₂Se-Based True Random Number Generator for Security Applications. *ACS Nano* **16**, 6847–6857 (2022).
9. Lanza, M. *et al.* Memristive technologies for data storage, computation, encryption, and radio-frequency communication. *Science* **376**, eabj9979 (2022).
10. Lemme, M. C., Akinwande, D., Huyghebaert, C. & Stampfer, C. 2D materials for future heterogeneous electronics. *Nat. Commun.* **13**, 1392 (2022).
11. Wen, C. *et al.* Advanced Data Encryption using 2D Materials. *Adv. Mater.* **33**, 2100185 (2021).
12. Glavin, N. R. *et al.* Emerging Applications of Elemental 2D Materials. *Adv. Mater.* **32**, 1904302 (2020).
13. Lai, Z. *et al.* Metastable 1T'-phase group VIB transition metal dichalcogenide crystals. *Nat. Mater.* **20**, 1113–1120 (2021).
14. Yuan, S. *et al.* Room-temperature ferroelectricity in MoTe₂ down to the atomic monolayer limit. *Nat. Commun.* **10**, 1775 (2019).
15. Keum, D. H. *et al.* Bandgap opening in few-layered monoclinic MoTe₂. *Nat. Phys.* **11**, 482–486 (2015).
16. Qi, Y. *et al.* Superconductivity in Weyl semimetal candidate MoTe₂. *Nat. Commun.* **7**, 11038 (2016).
17. Gerstner, W., Kistler, W. M., Naud, R. & Paninski, L. *Neuronal Dynamics*. (Cambridge University Press, 2014).

18. Zhang, F. *et al.* Electric-field induced structural transition in vertical MoTe₂- and Mo_{1-x}W_xTe₂-based resistive memories. *Nat. Mater.* **18**, 55–61 (2019).
19. Wang, Y. *et al.* Structural phase transition in monolayer MoTe₂ driven by electrostatic doping. *Nature* **550**, 487–491 (2017).
20. Zhang, K. *et al.* Raman signatures of inversion symmetry breaking and structural phase transition in type-II Weyl semimetal MoTe₂. *Nat. Commun.* **7**, 13552 (2016).
21. Yang, J. *et al.* Elastic and electronic tuning of magnetoresistance in MoTe₂. *Sci. Adv.* **3**, eaao4949 (2017).
22. Lin, Z. *et al.* Solution-processable 2D semiconductors for high-performance large-area electronics. *Nature* **562**, 254–258 (2018).
23. Yu, W. *et al.* High-Yield Exfoliation of Monolayer 1T'-MoTe₂ as Saturable Absorber for Ultrafast Photonics. *ACS Nano* **15**, 18448–18457 (2021).
24. Miller, D. A. B. *et al.* Band-Edge Electroabsorption in Quantum Well Structures: The Quantum-Confined Stark Effect. *Phys. Rev. Lett.* **53**, 2173–2176 (1984).
25. Liu, S. *et al.* Conduction Modulation of Solution-Processed 2D Materials. *Adv. Electron. Mater.* **10**, 2300799 (2024).
26. Kingman, J. F. C. *Poisson Processes*. (Clarendon Press, 1992).
27. Last, G. & Penrose, M. *Lectures on the Poisson Process*. (Cambridge University Press, 2017).
28. Liu, D., Liu, Z., Li, L. & Zou, X. A Low-Cost Low-Power Ring Oscillator-Based Truly Random Number Generator for Encryption on Smart Cards. *IEEE Trans. Circuits Syst. II Express Briefs* **63**, 608–612 (2016).
29. Dutta, P. & Horn, P. M. Low-frequency fluctuations in solids: 1/f noise. *Rev. Mod. Phys.* **53**, 497 (1981).
30. Van Der Ziel, A. Noise in solid-state devices and lasers. *Proc. IEEE* **58**, 1178–1206 (1970).
31. Ma, X. *et al.* Defects Induced Charge Trapping/De trapping and Hysteresis Phenomenon in MoS₂ Field-Effect Transistors: Mechanism Revealed by Anharmonic Marcus Charge Transfer Theory. *ACS Appl. Mater. Interfaces* **14**, 2185–2193 (2022).
32. Li, L., Lee, I., Youn, D.-H. & Kim, G.-H. Hopping conduction and random telegraph signal in an exfoliated multilayer MoS₂ field-effect transistor. *Nanotechnology* **28**, 075201 (2017).
33. Song, S. H., Joo, M.-K., Neumann, M., Kim, H. & Lee, Y. H. Probing defect dynamics in monolayer MoS₂ via noise nanospectroscopy. *Nat. Commun.* **8**, 2121 (2017).
34. Kelly, A. G., O'Suilleabhain, D., Gabbett, C. & Coleman, J. N. The electrical conductivity of solution-processed nanosheet networks. *Nat. Rev. Mater.* **7**, 217–234 (2021).
35. Ashcroft, N. W. & Mermin, N. D. *Solid State Physics*. (Cengage Learning, 2022).
36. Martin-Martinez, J., Diaz, J., Rodriguez, R., Nafria, M. & Aymerich, X. New Weighted Time Lag Method for the Analysis of Random Telegraph Signals. *IEEE Electron Device Lett.* **35**, 479–481 (2014).
37. Chowdhury, T. *et al.* Substrate-directed synthesis of MoS₂ nanocrystals with tunable dimensionality and optical properties. *Nat. Nanotechnol.* **15**, 29–34 (2020).
38. Zaman, J. & Ghosh, R. Review on fifteen statistical tests proposed by NIST. *J. Theor. Phys. Cryptogr.* **1**, 18–31 (2012).
39. Woo, K. S. *et al.* A Combination of a Volatile-Memristor-Based True Random-Number Generator and a Nonlinear-Feedback Shift Register for High-Speed Encryption. *Adv. Electron. Mater.* **6**, 1901117 (2020).

40. Kumar Sharma, D., Chidananda Singh, N., Noola, D. A., Nirmal Doss, A. & Sivakumar, J. A review on various cryptographic techniques & algorithms. *Mater. Today Proc.* **51**, 104–109 (2022).
41. Acosta, A. J., Addabbo, T. & Tena-Sánchez, E. Embedded electronic circuits for cryptography, hardware security and true random number generation: an overview. *Int. J. Circuit Theory Appl.* **45**, 145–169 (2017).
42. Dwork, C. Differential Privacy. in *Automata, Languages and Programming* (eds. Bugliesi, M., Preneel, B., Sassone, V. & Wegener, I.) 1–12 (Springer Berlin Heidelberg, Berlin, Heidelberg, 2006).
43. He, K., Zhang, X., Ren, S. & Sun, J. Deep residual learning for image recognition. in *Proceedings of the IEEE conference on computer vision and pattern recognition* 770–778 (2016).
44. Kvatinsky, S. *et al.* Models of memristors for SPICE simulations. in *2012 IEEE 27th Convention of electrical and electronics engineers in Israel* 1–5 (IEEE, 2012).
45. Li, Z., Liu, F., Yang, W., Peng, S. & Zhou, J. A Survey of Convolutional Neural Networks: Analysis, Applications, and Prospects. *IEEE Trans. Neural Netw. Learn. Syst.* **33**, 6999–7019 (2022).
46. Modine, F. A., Major, R. W., Choi, S. I., Bergman, L. B. & Silver, M. N. Polarization currents in varistors. *J. Appl. Phys.* **68**, 339–346 (1990).
47. Hartke, J. L. The three-dimensional Poole-Frenkel effect. *J. Appl. Phys.* **39**, 4871–4873 (1968).

Acknowledgements

Funding: GHH acknowledges support from CUHK (4055115), YL from SHIAE (RNE-p3-21), JFP and YYW from RGC (24200521), TM from PolyU (P0042991), GW from NSFC (12074033), SG from National Key Research and Development Program of China (2023YFB3208003), XLC from NSFC (62275117) and Shenzhen excellent youth program (RCYX20221008092900001).

Author contributions: YL, GHH designed the experiments. YL, PYL, YYW, ZHL, SWL, LKS, JFP, XYF performed the experiments. YL, PYL, GHH analyzed the data. YL, GHH prepared the figures. YL, GHH wrote the manuscript. All authors discussed the results from the experiments and commented on the manuscript.

Competing interests: The authors declare no competing financial interests.

Data and materials availability: The data that support the findings of this study are available from the corresponding authors upon request.

Figures

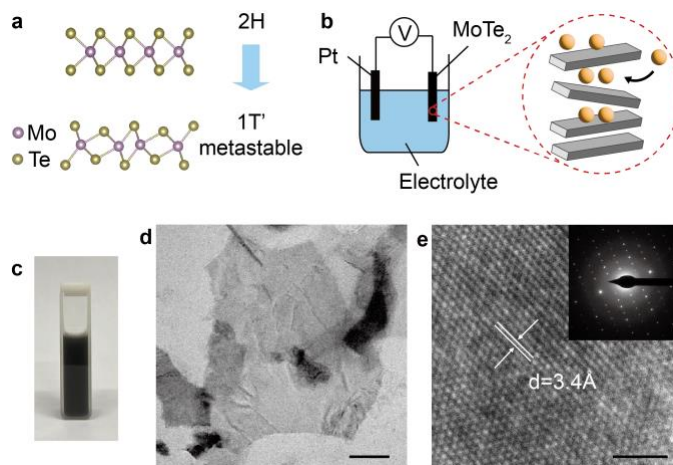


Figure 1. 1T' MoTe₂ by electrochemical exfoliation. (a) Crystalline structures of hexagonal 2H and distorted octahedral 1T' MoTe₂. (b) Schematic electrochemical exfoliation of MoTe₂, showing intercalation of molecular compounds between the MoTe₂ layers. Pt and MoTe₂ are used as the electrodes. (c) Dispersion of the exfoliated MoTe₂. (d, e) Transmission electron microscopic images and the selected electron diffraction pattern (inset of e) of the exfoliated MoTe₂ nanosheets, proving a distorted octahedral 1T' crystalline structure.

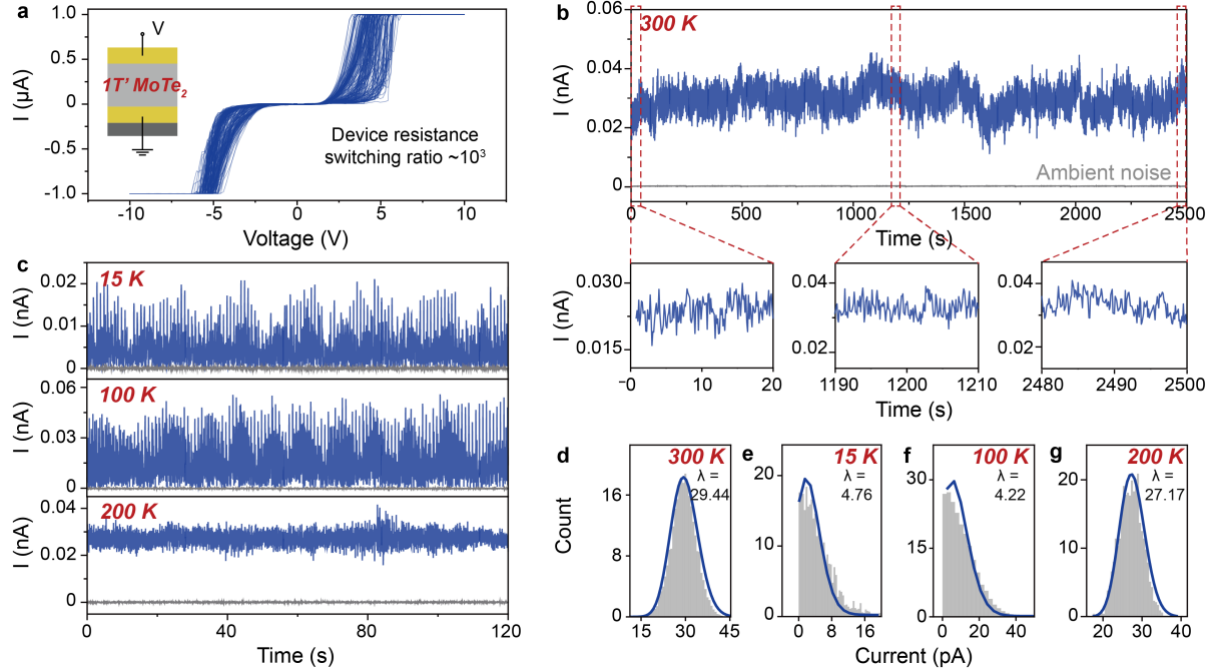


Figure 2. Conductance noise probing. (a) Current-voltage output for 100 cycles of a typical 1T' MoTe₂ device, showing random variations in the device resistance switching. The switching ratio is estimated as ~ 1424 between the averaged high and low device resistances. Inset shows the device structure. (b) Current output from the device at 300 K, and the current output details in the different short periods, showing stable conductance noise probed from 1T' MoTe₂. (c) Current output at low temperatures, showing stable conductance noise. The bias is 0.05 V for all the tests. See Fig. S3 for the output at the other bias conditions. Current output from a blank device is presented in grey for comparison. (d-g) Histograms and Poisson fittings of the current data points from (b) and (c), proving the conductance noise probed from 1T' MoTe₂ is a random process.

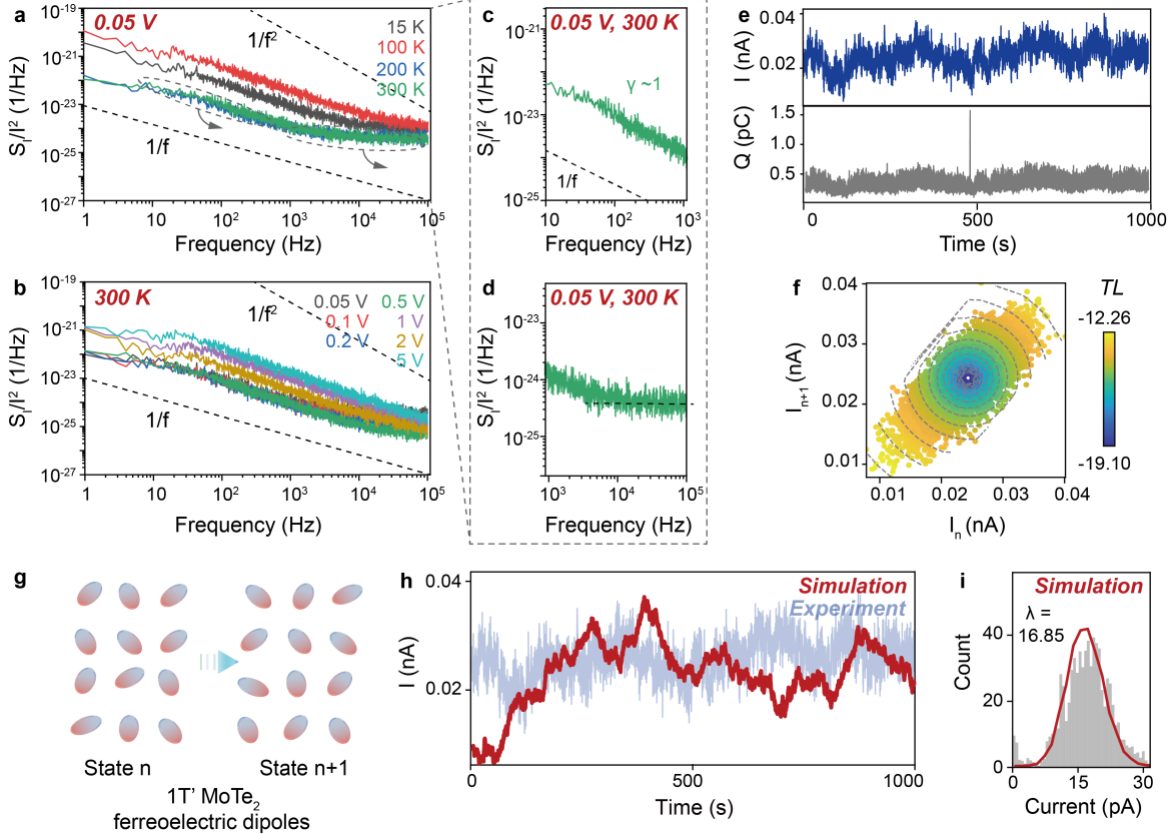


Figure 3. Origin of the conductance noise. Current power spectral density (PSD) of the 1T' MoTe₂ device at (a) 0.05 V and (b) 300 K, with (c, d) showing the PSD at low and high frequency regions for the 0.05 V, 300 K testing condition. PSD testing proves 1/f noise behavior for the conductance noise probed from 1T' MoTe₂. (e) Current output and the corresponding cumulative charge fluctuation of the 1T' MoTe₂ device at 0.05 V, 300 K. The cumulative charge is integrated during the sampling interval of 0.067 s. (f) Time-lag plot for the cumulative charge fluctuation, showing bimodal distribution along the diagonal, suggesting stronger correlations for the larger and smaller cumulative charge states to the next states. (g) Schematic n -th and $(n + 1)$ -th polarization states of the ferroelectric dipoles in 1T' MoTe₂ in our proposed conductance noise mechanism, showing random polarization of the ferroelectric dipoles. (h) Current output from Monte Carlo simulation on the random polarization of the ferroelectric dipoles, with the current output in (e) plotted as the background for comparison. (i) Histogram and Poisson fitting of the current data points from Monte Carlo simulation, indicating the conductance noise probed from 1T' MoTe₂ due to the random polarization of the ferroelectric dipoles is random and a reliable entropy source.

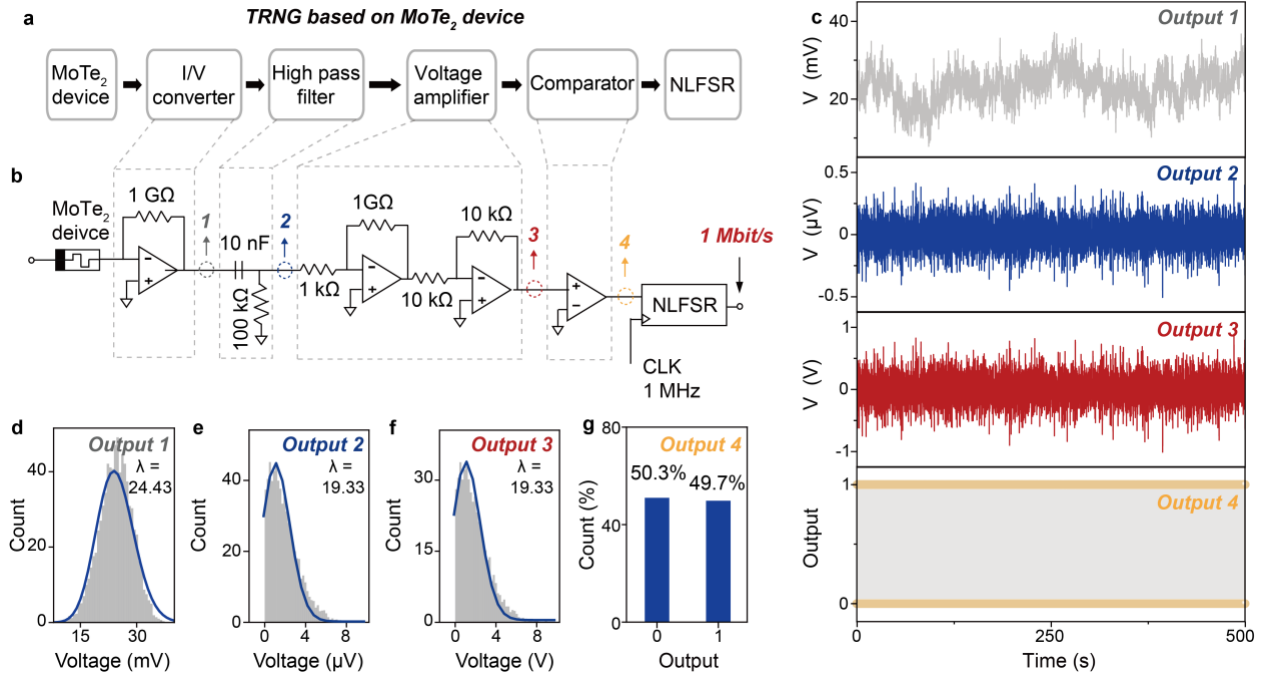


Figure 4. True random number generation. (a, b) Circuit design and diagram of the true random number generator (TRNG), consisting of the 1T' MoTe₂ device, I/V converter, high pass filter, voltage amplifier, comparator, and NLFSR. NLFSR (Fig. S7) is used to generate high-throughput random numbers from the seed, i.e. the true random numbers from *Port 4*. (c) The output obtained from the TRNG at *Port 1-4*, including the converted voltage output, the filtered voltage output, the amplified voltage output, and the generated true random numbers in a string of 0's and 1's. See Fig. S8 for the 0's and 1's string details. (d-f) Histograms and Poisson fittings of the data points from *Output 1-3* in (c), proving all the output are random processes. Note absolute values are taken from the negative data points in *Output 2* and *3* for the Poisson fittings. (g) Histogram of the 0's and 1's true random numbers in *Output 4* in (c), demonstrating a ratio of ~1:1.

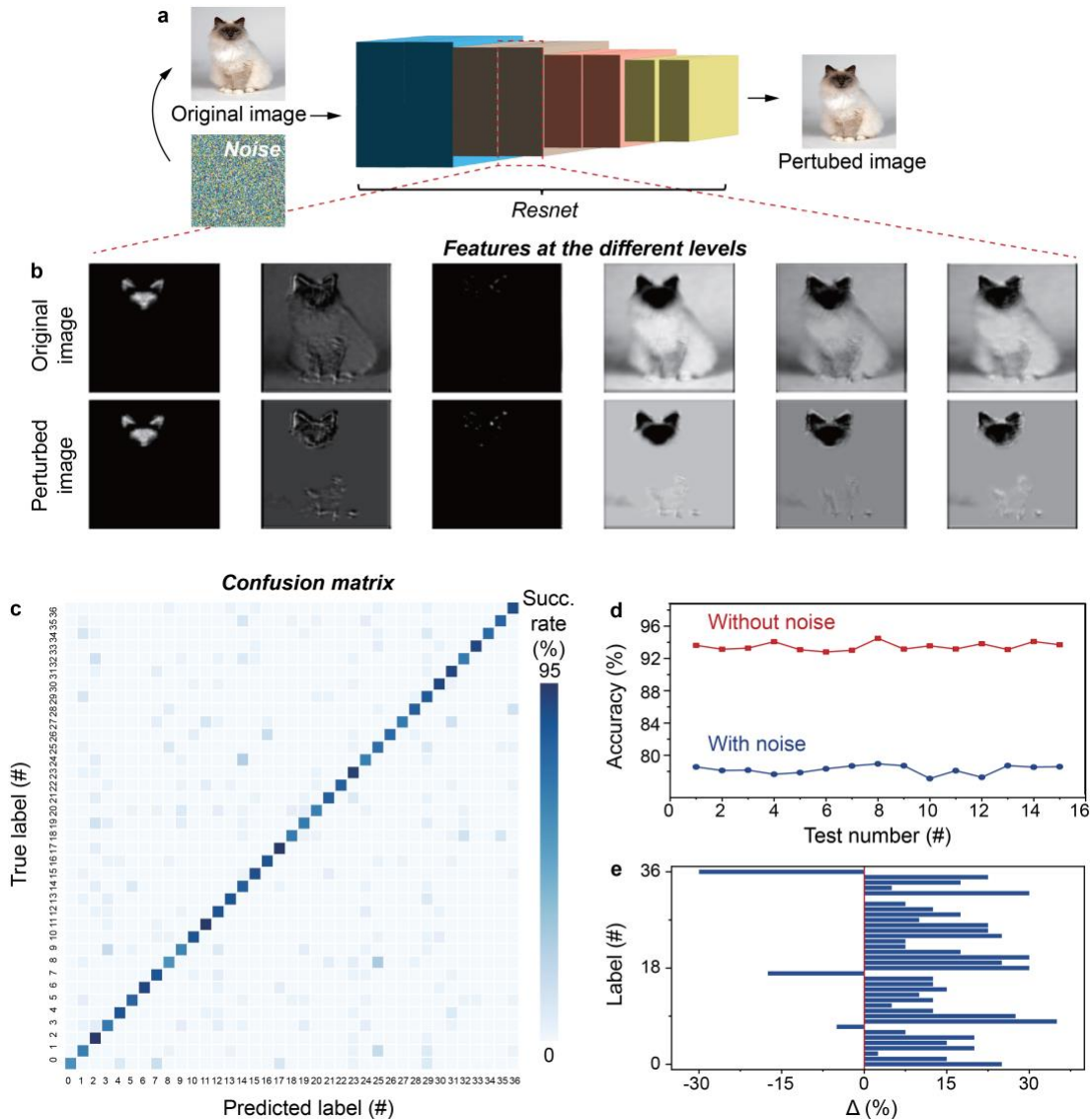


Figure 5. Interference and proffer safeguarding in neural networks. (a) Resnet variant architecture for cat recognition without and with noise perturbation. The noise map is produced using the high-throughput random numbers generated. (b) The cat images without and with noise perturbation at the intermediate convolution layers, showing that the perturbed images lose certain features of the cat throughout the convolution layers. (c) Confusion matrix for the Resnet variant recognition with noise perturbation. The scale corresponds to the success rate of the predicted labels. The x and y coordinates denote the predicted and true labels of the 37 classifications in the training dataset. (d) The accuracy with and without noise perturbation at the different test numbers. (e) The difference between the success rates in the confusion matrices with and without noise perturbation along the diagonal. The x coordinate denotes the difference in the success rate along the diagonal, and the y coordinate the 37 different classifications. The confusion matrix details with the success rate values are presented in Fig. S14.

Supplementary Figures and Tables

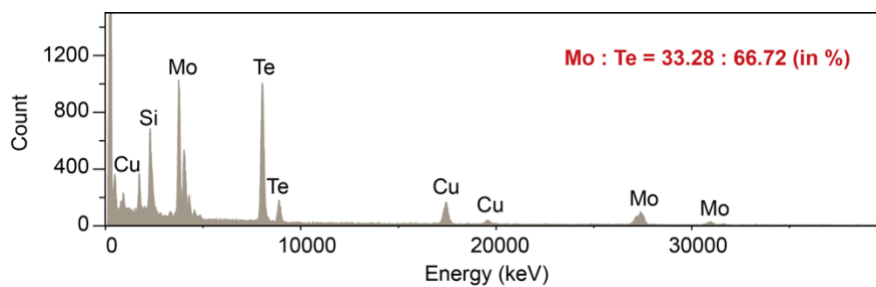


Figure S1. Energy dispersive X-ray spectrometry element mapping of the exfoliated 1T' MoTe₂ nanosheets. The ratio of the Mo and Te atoms is 33.28: 66.72 (in %), proving that there are minimal defects in the exfoliated 1T' MoTe₂ nanosheets.

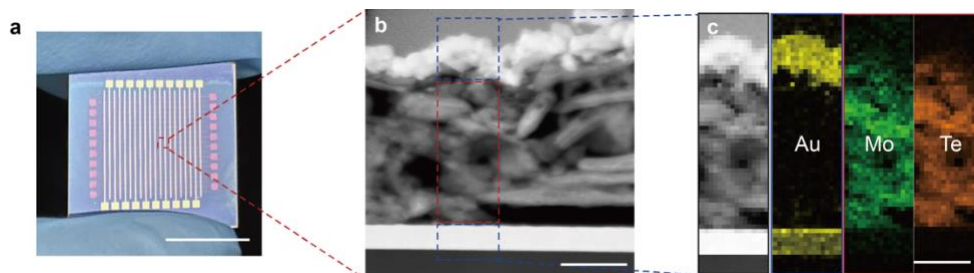


Figure S2. 1T' MoTe₂ devices. (a) Image of an array of 20 ×20 1T' MoTe₂ devices. Spin-coated 1T' MoTe₂ is sandwiched between the evaporated top and bottom gold electrodes to fabricate the devices. The device fabrication success rate is 100%. The substrate is Si/SiO₂. (b) Cross-sectional scanning electron microscopic image of a typical device, and (c) the corresponding elemental analysis of the selected areas for the Au, Mo, and Te elements, showing clear interfaces between the MoTe₂ layer and the electrodes. Scale bars – (a) 1 cm, (b) 300 nm, and (c) 300 nm.

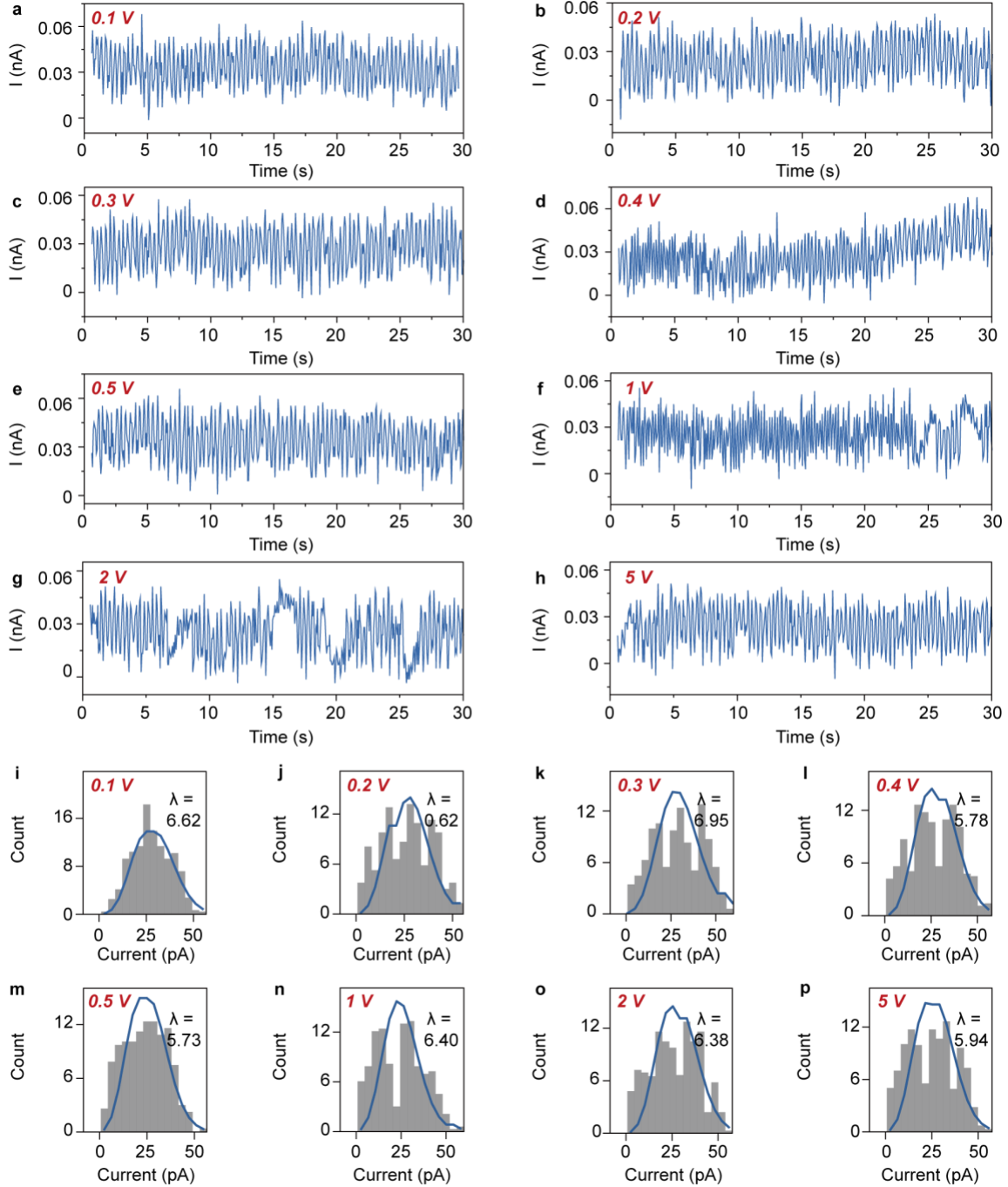


Figure S3. Conductance noise probing. (a)-(h) Current output of the 1T' MoTe₂ device at bias of 0.1 V, 0.2 V, 0.3 V, 0.4 V, 0.5 V, 1 V, 2 V, and 5 V. The temperature is 300 K. (i)-(p) The corresponding histograms and Poisson fittings of the current data points, proving the conductance noise in the 1T' MoTe₂ device measured at all the bias conditions is a random process and a reliable entropy source.

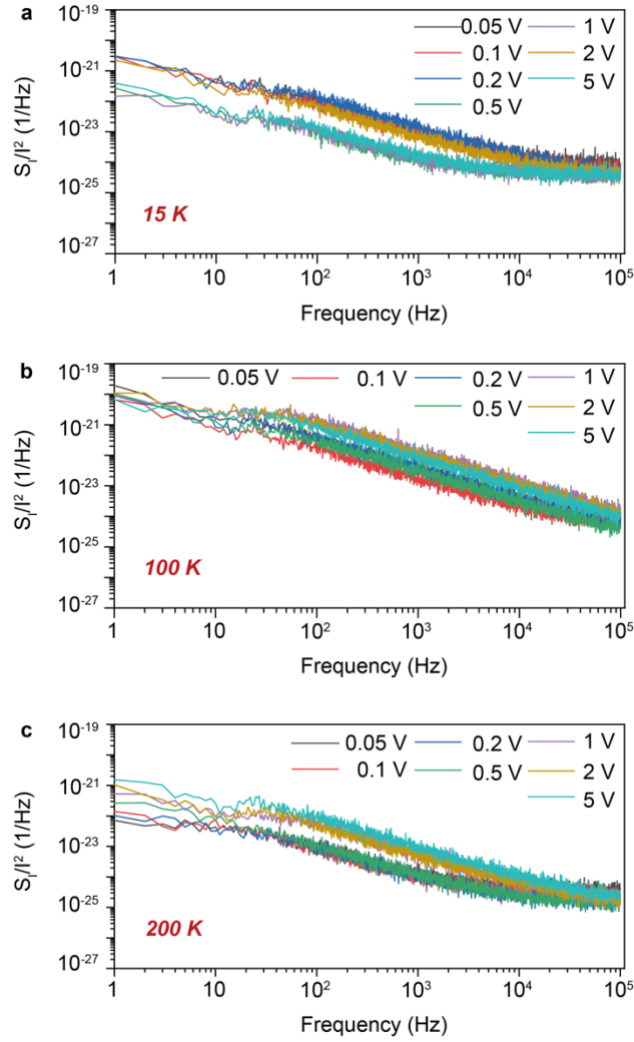


Figure S4. Current power spectral density (PSD) characterization of the 1T' MoTe₂ device at low temperatures. The PSD testing is conducted on the 1T' MoTe₂ device at a low temperature from 15 K to 300 K at the different bias conditions – (a) 15 K, (b) 100 K, and (c) 200 K. The testing proves 1/f noise in the device for all the temperature and bias testing conditions in the low-frequency region.

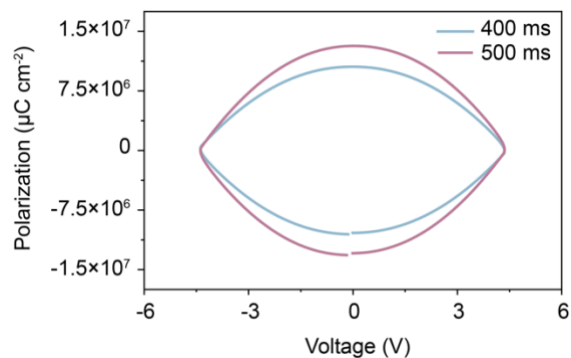


Figure S5. Ferroelectric polarization characterization of the 1T' MoTe₂ device. The ferroelectric polarization testing is conducted on a typical 1T' MoTe₂ device with a sweeping bias, showing no clear evidence of ferroelectric polarization. The test condition: $V_{\text{max}} = 5 \text{ V}$; Hysteresis speed = 400 ms/500 ms; Preset delay = 1,000 ms.

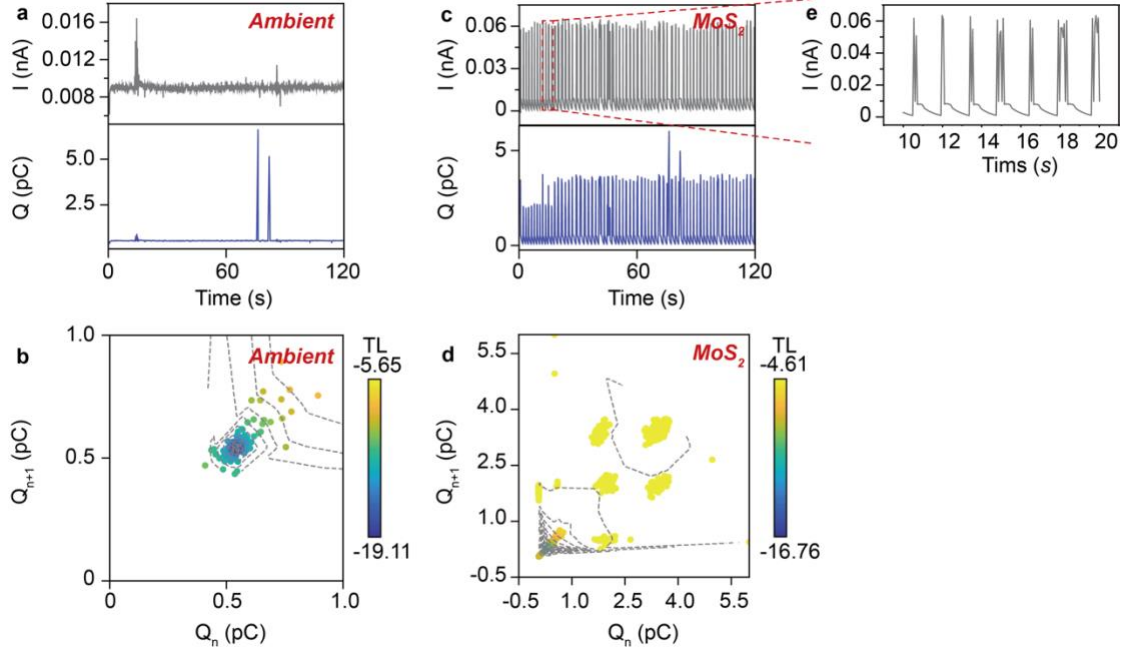


Figure S6. Control experiments on a blank device and a MoS_2 device. Current output and the corresponding cumulative charge fluctuations from (a) a blank device and (c) a MoS_2 device at 0.05 V, 300 K, with (e) showing the detailed current output from the MoS_2 device. MoS_2 is prepared by liquid-phase exfoliation^[1], and is then spin-coated and sandwiched between evaporated top and bottom gold electrodes to fabricate the MoS_2 devices. The device fabrication method and the device configuration are the same as that of the 1T' MoTe_2 devices. The current output of the MoS_2 device shows a distinct random switching behavior, proving random telegraph noise (RTN)^[2] from the MoS_2 device. The origin of the RTN is suggested to be attributed to the charge trapping and de-trapping at the defect sites in the MoS_2 material^[3,4]. The cumulative charge is integrated during the sampling time interval of 0.067 s. The time-lag plots for the cumulative charge fluctuations of (b) the blank device and (d) the MoS_2 device: the TL plot of the blank device establishes monostable aggregation with weak correlations in the cumulative charge states, meaning weak correlations in the noise states from the blank device; the TL plot of the MoS_2 device establishes random aggregation regions with strong correlations in the corresponding cumulative charge states, which may be a result of the charge trapping and de-trapping mechanism.

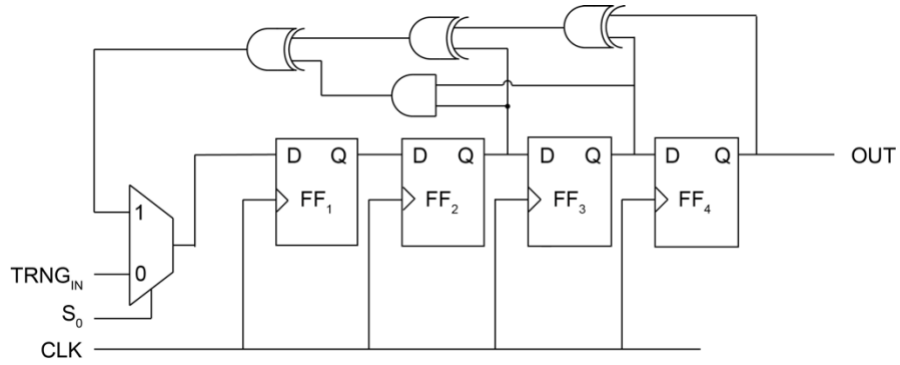


Figure S7. 4-bit nonlinear feedback shift register (NLFSR) circuit design. The NLFSR is used to generate high-throughput random numbers from the seed, i.e. the true random numbers, by setting a high clock frequency, e.g. 1 Mhz.

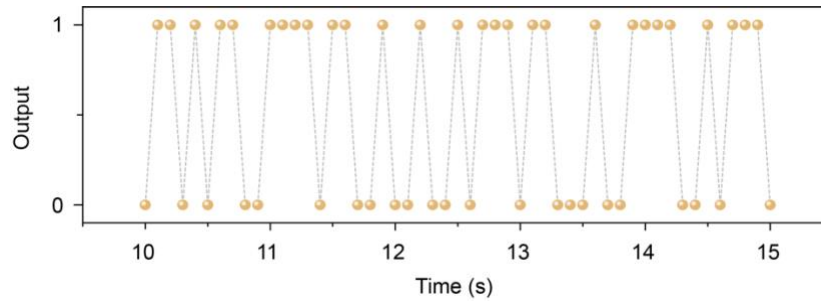


Figure S8. Random bit string of the 0's and 1's true random numbers generated from “port 4” during 10 to 15 seconds (the full time-scale true random number output is shown in Fig. 4c). It is shown that the 0's and 1's true random numbers are generated in a random distribution.

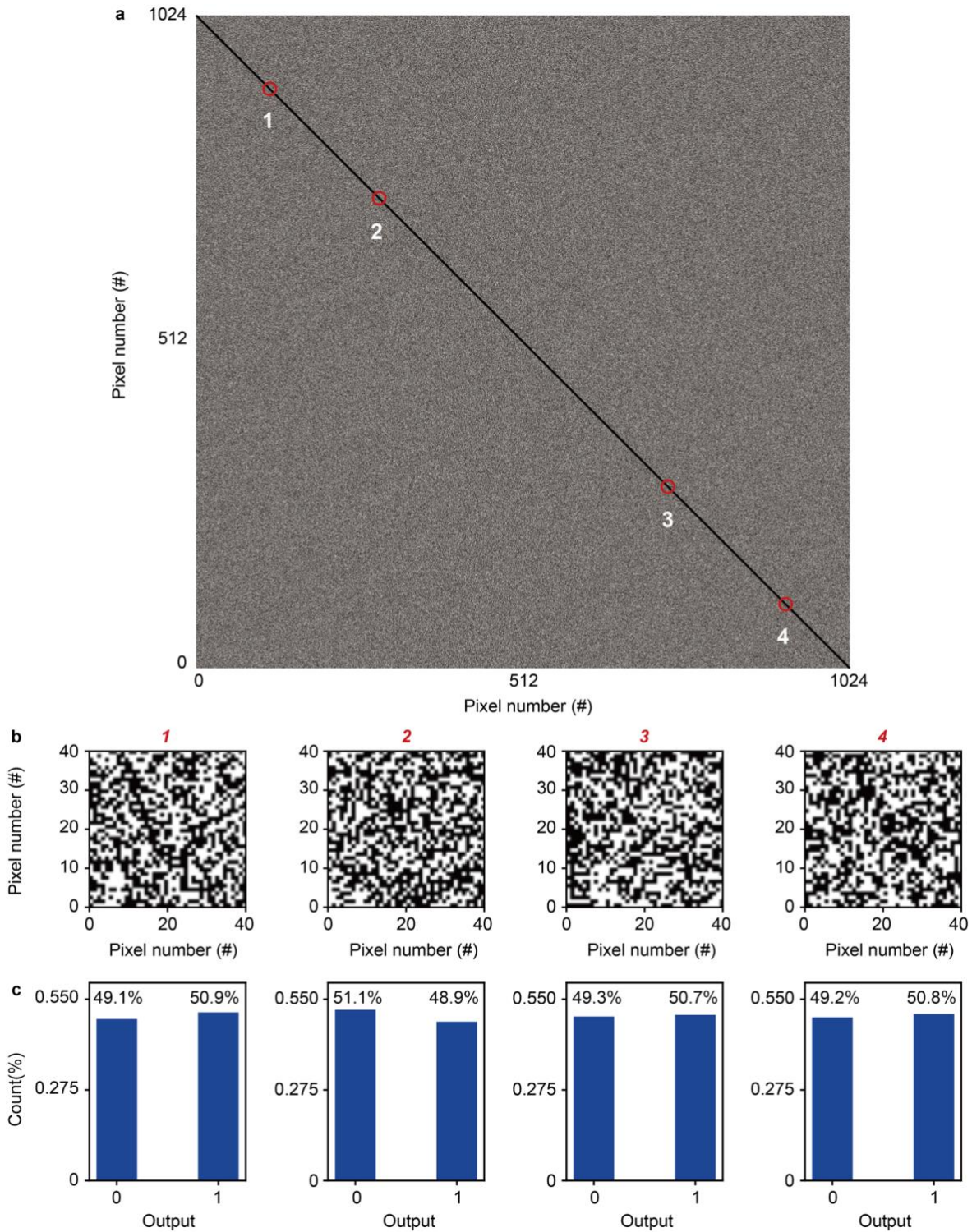
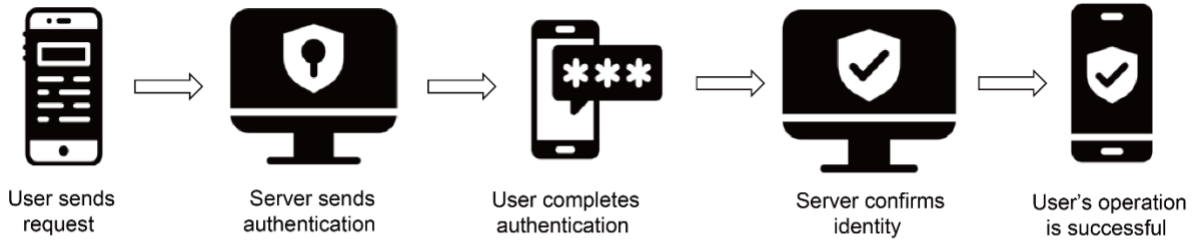


Figure S9. A 1024*1024 bitmap generated using the high-throughput random numbers. To plot the bitmap, the string of the high-throughput random numbers in 0's and 1's digits fills the bitmap sequentially from (0, 0) to (1024, 1024). (a) High-data-volume bitmap. (b) Four randomly selected bitmap regions along the diagonal of the high-data-volume bitmap. (c) The corresponding histograms showing the distributions of the 0's and 1's. The ratios of the 0's and 1's are close to 1 to 1.

a: One-time password



b: Strongly randomized password

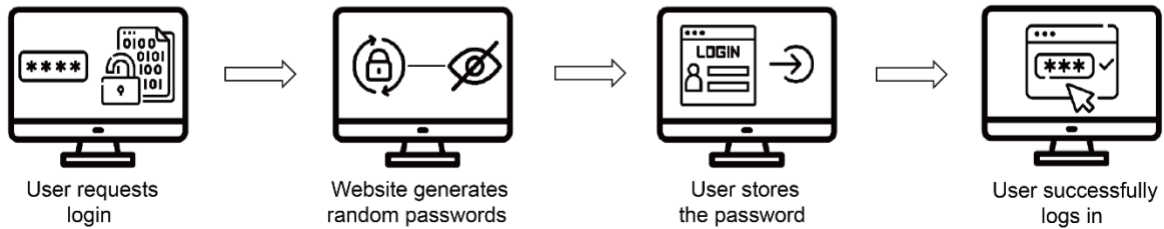


Figure S10. Password generation. (a) Schematic generation and the use of one-time password (OTP)^[5]. OTP is a unique password code that is valid for only one login/transaction session. It is often used as a second factor in two-factor authentication (2FA) and multi-factor authentication (MFA) systems^[5]. (b) Schematic generation and the use of strongly randomized passwords. Strongly randomized passwords can be stored in systems for the applications that require a high level of password security.

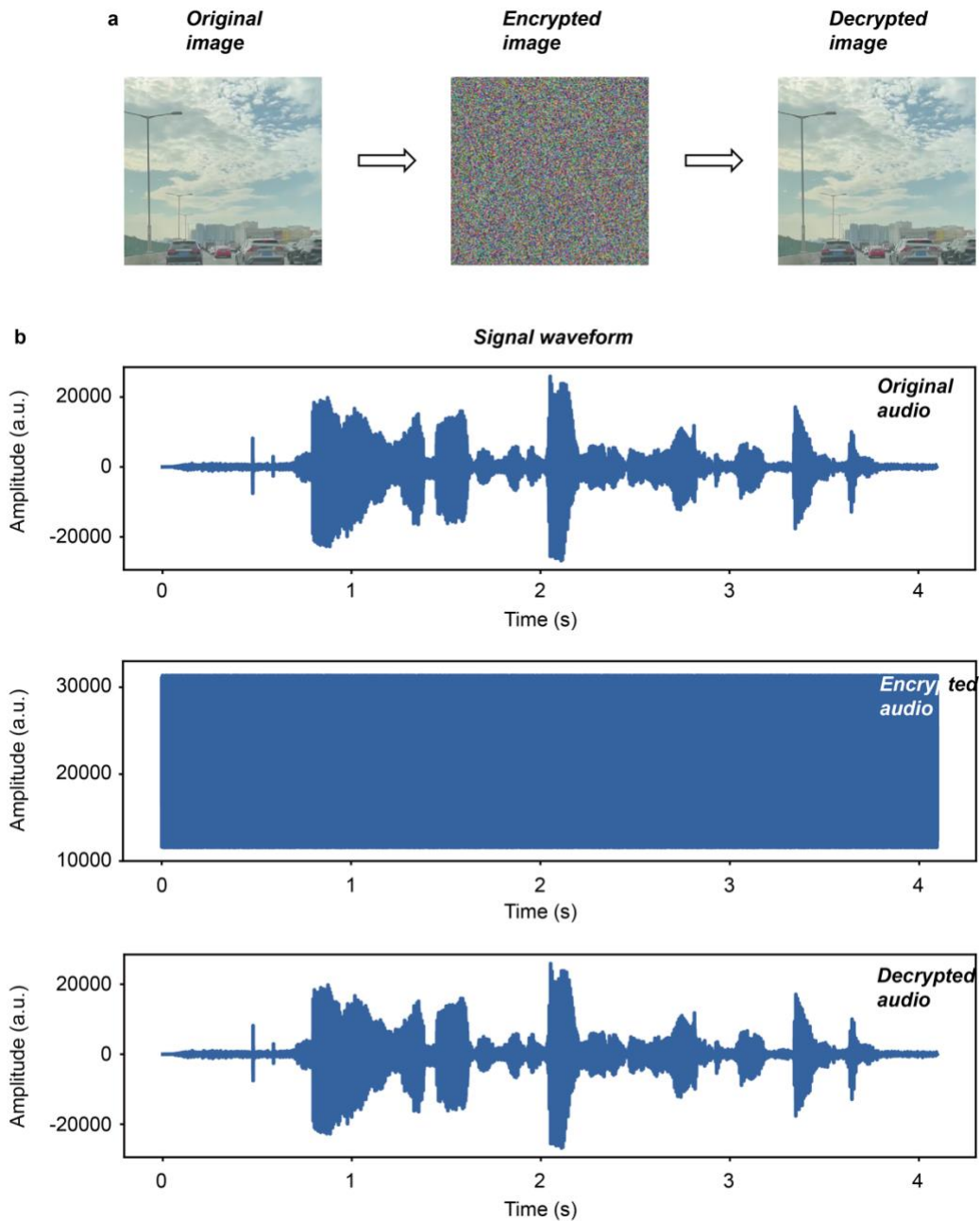


Figure S11. Data encryption. (a) Encryption and decryption of an image. The encryption and decryption are conducted by performing the common encryption/decryption operations (e.g. AES encryption/decryption method ^[6]) on the pixels using the high-throughput random numbers generated. (b) Acoustic spectrograms for audio encryption and decryption, showing a four-second audio, the audio after bit-by-bit encryption, and the audio after decryption.

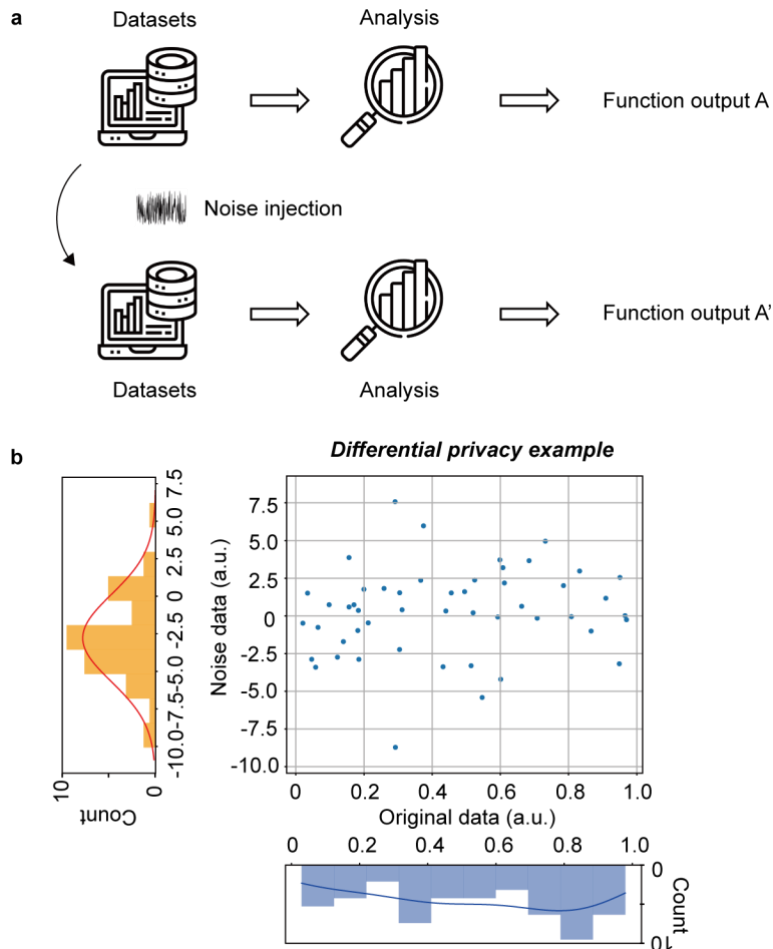


Figure S12. Differential data safeguarding strategy. (a) Differential data privacy workflow. Differential data privacy is a robust framework used in statistical and machine learning analysis of datasets [7]. The core idea is to ensure that the release of the data (or the statistics derived from the data) does not compromise the privacy of any individuals in the datasets, and that the datasets with the noise perturbation retain the key features. (b) A case example showing injecting noise to a dataset for data privacy protection. The left plot shows the noise data, and the bottom plot the original raw data. The noise data is injected into the original data. An example using the differential privacy protection of biometric information such as facial features in neural networks is presented in Fig. 5.

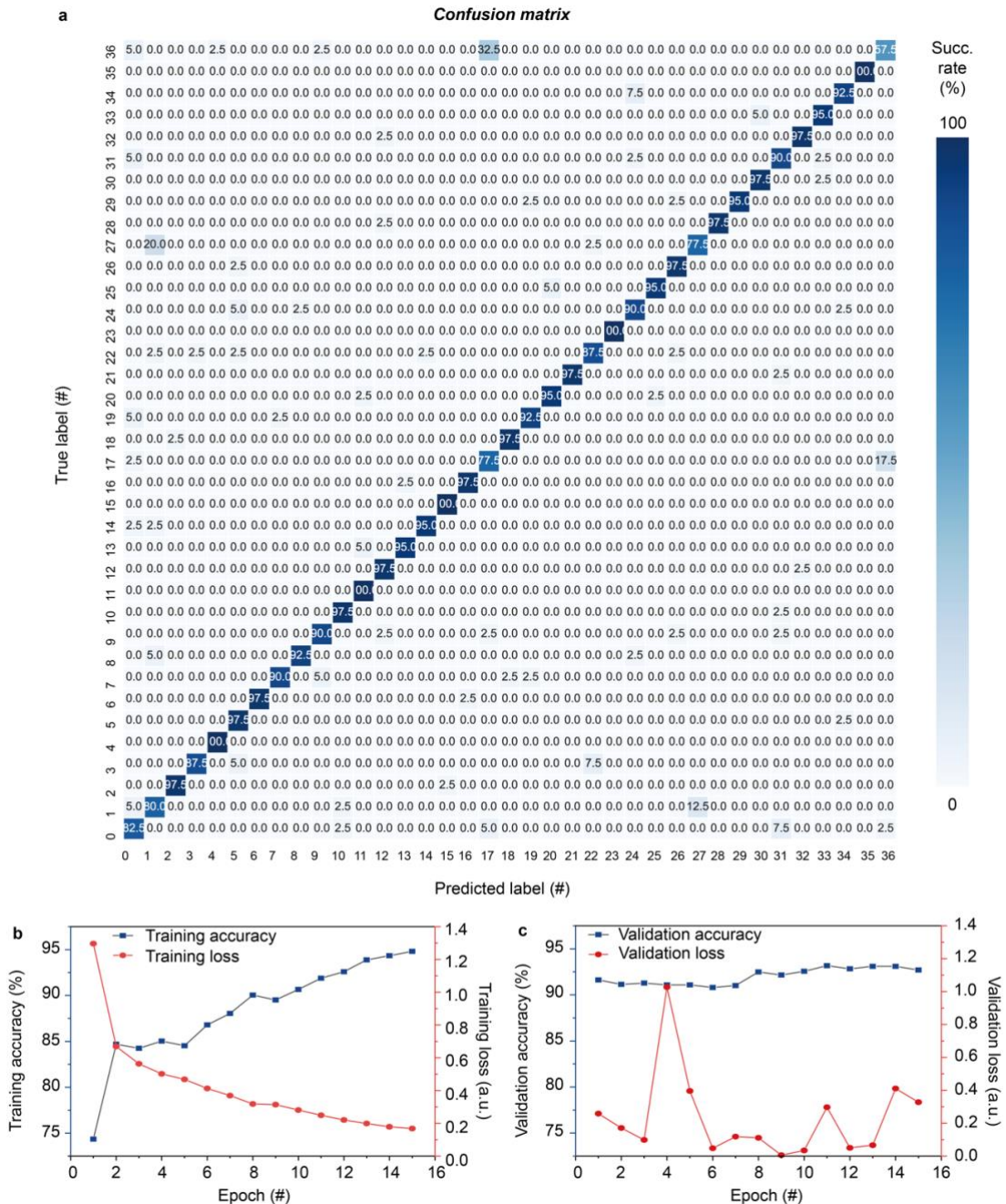


Figure S13. Confusion matrix without noise perturbation and the training performance of the Resnet model. (a) Confusion matrix without noise perturbation. The x and y coordinates denote the predicted and true labels of the 37 different classifications in the training dataset, i.e. the Oxford pet-iii dataset. The scale (i.e. the success rate of classification) corresponds to the ratio of the number of the correctly predicted labels to the number of the true labels. The values as shown in the confusion matrix represent the success rate. The success rate shows that the trained Resnet variant achieves a good performance ($\sim 92\%$). (b) The training accuracy and training loss of the Resnet variant. (c) The validation accuracy and validation loss of the Resnet variant. Based on the performance of (b) and (c), it can be concluded that the Resnet variant is well-trained for the Oxford pet-iii dataset.

Table S1. NIST test of the true random numbers.

	<i>P-value</i>	<i>Success</i>	<i>Post-processing</i>
<i>Approximate entropy</i>	1.0	Success	No
<i>Block frequency</i>	0.824	Success	No
<i>Cumulative sums</i>	0.728, 0.526	Success	No
<i>FFT</i>	0.041	Success	No
<i>Frequency</i>	0.823	Success	No
<i>Linear complexity</i>	-	-	Limited throughput
<i>Longest run</i>	0.445	Success	No
<i>Non overlapping template</i>	0.999	Success	No
<i>Overlapping template</i>	-	-	Limited throughput
<i>Random excursions</i>	-	Success	No
<i>Random excursions variant</i>	-	Success	No
<i>Rank</i>	-	-	Limited throughput
<i>Runs</i>	0.017	Success	No
<i>Serial</i>	0.499, 0.499	Success	No
<i>Universal</i>	-	-	Limited throughput

Table S2. NIST test of the high-throughput random numbers.

	<i>P-value</i>	<i>Proportion</i>	<i>Success</i>	<i>Post-processing</i>
<i>Approximate entropy</i>	0.409	1	Success	No
<i>Block frequency</i>	0.373	1	Success	No
<i>Cumulative sums</i>	0.047	0.97	Success	No
<i>FFT</i>	0.500	1	Success	No
<i>Frequency</i>	0.057	0.98	Success	No
<i>Linear complexity</i>	0.371	1	Success	No
<i>Longest run</i>	0.965	1	Success	No
<i>Non overlapping template</i>	0.999	1	Success	No
<i>Overlapping template</i>	0.873	1	Success	No
<i>Random excursions</i>	0.525	1	Success	No
<i>Random excursions variant</i>	0.428	1	Success	No
<i>Rank</i>	0.696	0.99	Success	No
<i>Runs</i>	0.630	1	Success	No
<i>Serial</i>	0.607	1	Success	No
<i>Universal</i>	0.425	1	Success	No

Supplementary References

1. Hu, G. et al. A general ink formulation of 2D crystals for wafer-scale inkjet printing. *Science Advances* **6** 5029–5041.
2. Kogan, S. Random telegraph noise in microstructures. *Physical review letters* **81**, 2986 (1998).
3. Song, S. H., Joo, M.-K., Neumann, M., Kim, H. & Lee, Y. H. Probing defect dynamics in monolayer MoS₂ via noise nanospectroscopy. *Nature communications* **8**, 2121 (2017).
4. Ma, X. et al. Defects induced charge trapping/detrapping and hysteresis phenomenon in MoS₂ field-effect transistors: Mechanism revealed by anharmonic marcus charge transfer theory. *ACS Applied Materials & Interfaces* **14**, 2185–2193 (2022).
5. Ometov, A. et al. Multi-factor authentication: A survey. *Cryptography* **2**, 1 (2018).
6. Standards, N. I. of et al. *Advanced Encryption Standard (AES)*. (2001)
7. Dwork, C. Differential Privacy. in *Automata, Languages and Programming* (eds. Bugliesi, M., Preneel, B., Sassone, V. & Wegener, I.) 1–12 (Springer Berlin Heidelberg, Berlin, Heidelberg, 2006).